Boreal, Temperate, and Tropical Forests as Vicarious Calibration Sites for Spaceborne Microwave Radiometry

John Xun Yang, *Student Member, IEEE*, Darren S. McKague, *Member, IEEE*, and Christopher S. Ruf, *Fellow, IEEE*

***Abstract*—We develop methods of using boreal, temperate, and tropical forests as vicarious calibration sites for spaceborne microwave radiometers. The extended sites and improved calibration techniques enable examining warm-scene performances as a complement to cold scenes over the ocean, providing information about scan-dependent biases, detecting and correcting possible calibration errors, and intercalibrating different radiometers. Specifically, this paper shows results as follows. Warm-scene calibration is expanded beyond previously utilized sites in the Amazon rainforest to include inland boreal and temperate forests, as well as forests in coastal and island regions. These additional sites increase the available warm-scene sample size by a factor of 30 compared with using Amazon rainforests alone, allowing more accurate and statistically robust calibration. In addition, their widespread near-global distribution enables near-continuous monitoring of radiometer performance, e.g., with a temporal resolution of almost once per day. Accurate warm-end vicarious calibration enables or enhances several new capabilities for radiometer characterization. Scan-dependent calibration biases that are present at the high end of a radiometer's dynamic range can, for the first time, be reliably detected and characterized. Using this method, we are able to detect the along-scan magnetic interference and edge-of-scan biases that are present in Global Precipitation Measurement Microwave Imager (GMI) observations at warm brightness temperatures (TBs). Our techniques are able to detect and characterize very small calibration anomalies, e.g., a scan-dependent error in GMI with a peak-to-peak amplitude of 0.1 K. In general, scan-dependent performance and antenna pattern correction can be improved with better constraints at both the high and low ends of on-Earth observed TBs. Regional dependence and seasonal changes in the brightness and predictability of the forested calibration sites are detected and characterized. Calibration exhibits a dependence on latitude, most significantly at water vapor channels, where tropical regions are different from middle and high latitudinal regions. Although the root cause is still under investigation, its presence suggests that using limited sites could result in undesirable latitude-dependent calibration biases. The distribution of calibration sites shifts seasonally, which results from green-up of the vegetation canopy in summer and defoliation in winter, and from snow contamination.**

***Index Terms*—Forest, in-flight vicarious calibration, microwave radiometry, warm scene.**

Manuscript received January 6, 2015; revised April 13, 2015; accepted August 8, 2015. Date of publication September 15, 2015; date of current version January 19, 2016. This work was supported in part by the National Aeronautics and Space Administration under Grant NNX13AG70G.

The authors are with the Department of Climate and Space Sciences and Engineering, University of Michigan, Ann Arbor, MI 48109 USA (e-mail: johnxun@umich.edu; dmckague@umich.edu; cruf@umich.edu).

Color versions of one or more of the figures in this paper are available online at http://ieeexplore.ieee.org.

Digital Object Identifier 10.1109/TGRS.2015.2472532

I. Introduction

In-flight vicarious calibration using on-Earth targets is important for spaceborne microwave radiometers. Although prelaunch calibration is performed and radiometers have onboard calibration systems, further in-flight calibration is necessary to monitor and improve radiometer performance. Vicarious calibration is necessary to monitor possible drifts in the onboard calibration system after launch, as well as errors in the antenna pattern correction (APC) [1]. The onboard radiometer can be affected, for example, by the spacecraft itself due to obstruction of the antenna field of view (FOV) [2]. A slightly emissive antenna will add error to the observed radiance as antenna physical temperature changes with the orbit [3]–[5]. As the radiometer spins, scan-dependent anomalies can occur because of antenna beam blockage and other instrumental effects [5], [6]. The development of algorithms to convert antenna temperature (TA) into Earth-scene brightness temperature (TB) needs in-flight vicarious calibration to derive empirical correction parameters [5], in which issues such as TB-dependent errors can happen but can be identified and resolved through in-flight calibration [7]. Finally, intercalibration relies heavily on vicarious calibration so that different radiometers can be reconciled to produce consistent results for long-term climate data records [8], [9].

Warm-scene vicarious calibration is an important part of in-flight calibration. Earth-scene TBs have a roughly bimodal probability distribution. The cold TB from the ocean and the warm TB from the land dominate the distribution, and cryosphere and coastal transition regions provide a smaller percentage of intermediate TBs. Calibration errors can have dependence on TBs because of scan-dependent interference, APC errors, uncorrected radiometer nonlinearity, and simulation errors [7]. Current vicarious cold calibration uses clear-sky ocean scenes that cover a limited part of the full TB dynamic range [5], [8], [10]–[12]. For example, the 10-GHz horizontal polarization TBs of a conical scanning radiometer has a typical full range from 80 to 290 K, whereas the clear-sky ocean TBs ranges from 80 to 100 K. As a result, empirical corrections derived from cold scenes alone may not work well for a warm scene [7]. For missions such as the Global Precipitation Measurement (GPM), warm-scene calibration is particularly important because precipitating scenes are considerately warmer than clear-sky ocean scenes at lower microwave frequencies where scattering from ice is not significant. Thus, both cold- and warm-scene calibrations are necessary.

0196-2892 © 2015 IEEE. Personal use is permitted, but republication/redistribution requires IEEE permission.
See http://www.ieee.org/publications_standards/publications/rights/index.html for more information.

Modeling warm-scene emission is more difficult than cold scenes. The emissive properties of ocean and fresh water are generally well understood and easier to model than those of warm scenes. Land properties are more complex and uncertain. Land scenes differ significantly between different land types. Even in a limited terrestrial region, with the same surface type, TBs can be very inhomogeneous. Land scenes can also have a large diurnal and seasonal variability. It is more difficult to characterize the dependence of land emissivity on polarization, frequency, and Earth incidence angle (EIA). As a result, warm-scene calibration has to date provided only limited usable data and has been unable to provide the continuous radiometer monitoring necessary to reliably resolve scan-dependent calibration anomalies at warm-scene TBs.

Among different land types, forests have been found as useful vicarious calibration sites [2], [13]–[15]. The branches and leaves of dense forests form an optically thick canopy, hiding the ground that is more difficult to model. An optically thick forest canopy has near-blackbody properties of high emissivity and small dependence on polarization and EIA. Specifically, the emissivity of thick canopies has predictable frequency dependence in the microwave spectrum [16], [17]. Emissivity increases with frequency to a peak at about 10 GHz, then decreases slightly at higher frequencies. This is because lower frequencies have greater penetration through the canopy, whereas higher frequencies tend to scatter more. The forest emissivity is insensitive to incidence angle according to both observation and modeling [15]–[17]. These predictable properties enable the modeling of forest canopies.

The Amazon rainforest has large areas of thick canopies appropriate for calibrating spaceborne radiometers with large FOVs. Brown and Ruf [14] identified two areas of water-free Amazon rainforests and developed an empirical model to capture the diurnal and seasonal changes of TBs using Special Sensor Microwave/Imager data. These two areas have since been used as the warm calibration site in a number of studies. McKague *et al.* [2] combined both warm Amazon and cold ocean scenes to examine edge-of-scan FOV obstructions for WindSat. Biswas *et al.* [13] used the Amazon rainforest as one of their calibrations sites for intercalibration between Thematic Mapper Imager and WindSat. Mo [15] studied TBs over the Amazon rainforest using the cross-track scanning radiometer AMSU-A. These studies demonstrate the value of the Amazon rainforest as a reliable warm-scene calibration site.

There are two major limitations of current warm-scene calibration. First, the numbers of usable sites are limited. Compared with the amount of data from the ocean, the Amazon rainforest provides too few data for many types of statistical analyses or for continuous monitoring. The situation is even worse for intercalibration, where different radiometers with different orbits need to simultaneously overpass the same region, causing further reduction in data availability. Second, reliable scan-dependent calibration information is not available. This is due not only to the limited data availability but also to problems of surface inhomogeneity. Forests are not as homogeneous as the ocean, which increases the scatter in along-scan TBs and covers small error signals due to noise. Further investigation is needed to handle the problem of inhomogeneity.

In this paper, we develop methods to address the current challenges in warm-scene calibration. GMI and WindSat data are used for demonstration. This paper is organized as follows. Section II describes the methodology for identification of new vicarious sites and development of improved calibration techniques. In Section III, we apply our method to calibrate GMI in an absolute sense and to intercalibrate it using WindSat as the reference radiometer. Conclusions are presented in Section IV.

II. Methodology

A. Data and Instrument Specifications

WindSat is a conical scanning polarimetric microwave radiometer aboard the Coriolis satellite launched on January 6, 2003 [18]. It has 22 channels at five frequencies. The 10.7, 18.7 and 37 GHz are fully polarimetric, with each frequency having vertical (V), horizontal (H), $+45^\circ$, -45°, left-hand circular, and right-hand circular polarizations. The 6.8- and 23.8-GHz channels are dual-polarized (V and H only). WindSat's EIA ranges from 50° to 55°. WindSat has been well calibrated and has shown satisfying performance since its operation [18]–[20].

The GPM Microwave Imager (GMI) is a conical scanning microwave radiometer aboard the GPM core observatory launched on February 28, 2014 [21]. It has 13 channels at eight frequencies. The 10.65, 18.7, 36.64, 89, and 166 GHz have both V- and H-polarization channels, and 23.8, 183.31 ± 3, and 183.31 ± 7 GHz have V polarization only. EIAs are about 52.8° from 10.65 to 89 GHz, and 49.19° from 166 to 183.31 GHz, respectively.

Coincident channels between GMI and WindSat are intercalibrated in this paper. These channels are listed in Table I. The GMI data are archived and distributed by the NASA Precipitation Processing System [22]. Since the launch and operation of GMI, a number of calibrations have been developed and applied. The group at the University of Michigan is an member of the Intersatellite Radiometer Calibration Working Group (XCAL) team and has participated in the GMI calibration and conducted independent calibration work [7], [23], [24] (http://www.gpm-x-cal.info/). In addition, the manufacturers of the GMI instrument supplied a calibration algorithm based on prelaunch characterization of the instrument [10]. A number of calibration corrections have been developed and applied to GMI data since its launch. In this paper, version 03A (V03A) of the level 1C data is used. V03A data do not apply along-scan correction, which allows us to examine along-scan anomalies. The V03A data were created for March–August 2014 and then discontinued since further calibration adjustment including along-scan corrections have been applied in later data versions. The WindSat data are version 2.0.0 of the sensor data record [18]. Data from March through August of 2014 are used.

We also use the National Centers for Environmental Prediction (NCEP) Final (FNL) Tropospheric Analyses data to obtain geophysical parameters, including surface and atmospheric profiles. NCEP FNL data have a $1^\circ \times 1^\circ$ horizontal resolution, 26 vertical layers, and 6-h temporal resolution [25].

TABLE I
SPECIFICATIONS OF COINCIDENT CHANNELS BETWEEN GMI AND WINDSAT. THE COLLOCATION TIME DIFFERENCE IS SET AS 1-h IN THIS PAPER

Channel (GHz)	GMI	10.65V	10.65H	18.7V	18.7H	23.8V	36.64V	36.64H
	WindSat	10.7V	10.7H	18.7V	18.7H	23.8V	37V	37H
Bandwidth (MHz)	GMI	100	100	200	200	400	1000	1000
	WindSat	300	300	750	750	500	2000	2000
3dB size (km×km)	GMI	26×43	26×43	15×25	15×25	12×20	11×18	11×18
	WindSat	25×38	25×38	16×27	16×27	20×30	8×13	8×13

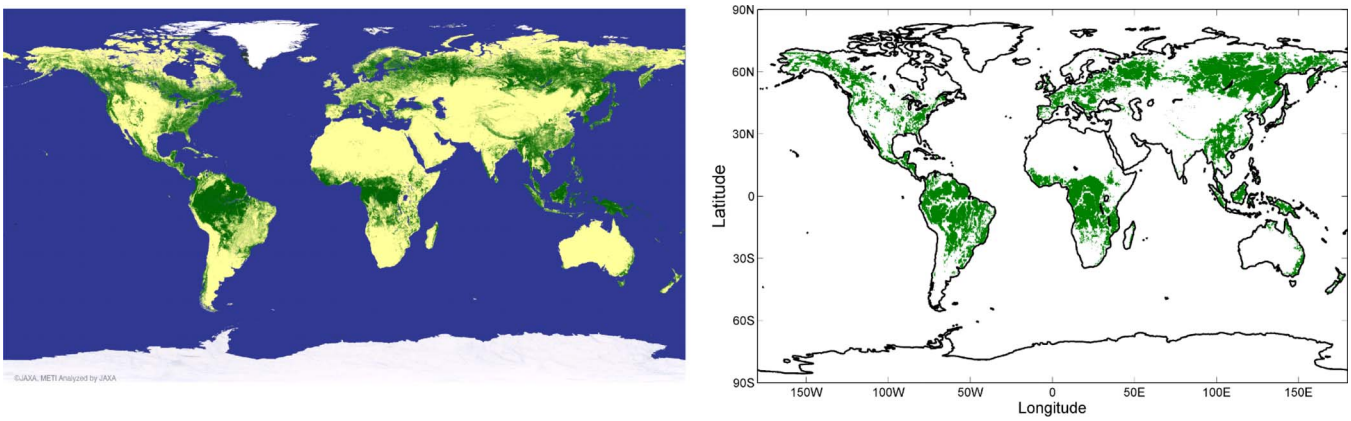


Fig. 1. Comparison between (left) the forest distribution from PALSAR and (right) the distribution of vicarious calibration sites based on GMI polarization difference. The identified sites correspond well to forested regions.

B. Method to Determine Vicarious Calibration Sites

As described by Brown and Ruf [9], a simple but effective method for identifying useful calibration sites is to consider their "polarization difference," i.e., the mean difference over a region between the TB at V and H polarizations for a common frequency. Both model [16] and measurements [14], [17] show that forests have small polarization difference compared with other land types. When microwave radiances from forests are mixed with signals from other sources such as bare soil, water, or snow, the polarization difference tends to increase. Therefore, a small polarization difference indicates optically thick forest canopies appropriate for calibration. An effective filter is found to be

$$\begin{aligned} \mathrm{TB_V} - \mathrm{TB_H} &\leq 3K, f < 22\ \mathrm{GHz} \\ \mathrm{TB_V} - \mathrm{TB_H} &\leq 2.5, K, f >= 22\ \mathrm{GHz} \end{aligned} \quad (1)$$

where $\mathrm{TB_V}$ and $\mathrm{TB_H}$ are TBs at V and H polarizations, respectively, and f is frequency.

Fig. 1 shows a map of GMI polarization difference compared with a forest map derived from the phased-array-type L-band SAR (PALSAR) measurements. The PALSAR plot shows the annual forest distribution in 2009, provided by the Japan Aerospace Exploration Agency as an Advanced Land Observing Satellite (ALOS) product [26]. There is a pronounced similarity between the GMI polarization difference and forest distribution. Fig. 2 further shows the distribution of different forest species: boreal, temperate, and tropical forests (http://www.ucar.edu/news/features/forests/). The forest species have latitudinal dependence. We will use these maps to define a group of calibration regions.

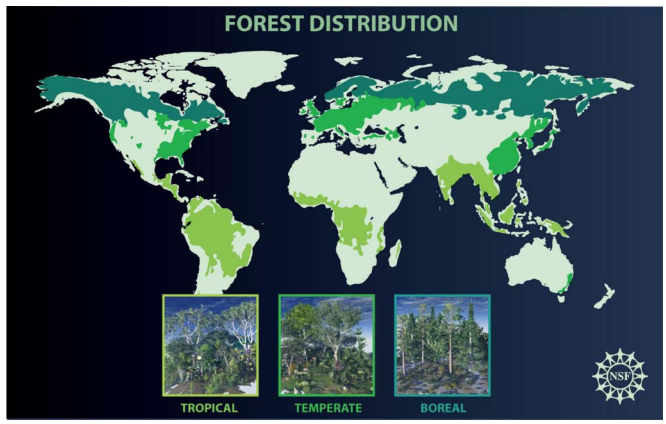


Fig. 2. Forest distributions of boreal, temperate, and tropical species (http://www.ucar.edu/news/features/forests/).

C. Models of Radiative Transfer, Canopy Emissivity, and Intercalibration

The TB at the top of atmosphere (TOA) can be written as [1]

$$\begin{aligned} \mathrm{TB} = \varepsilon T \exp(-\tau \sec\theta) + \mathrm{TB_{up}} + (1-\varepsilon)\exp(-\tau\sec\theta)\mathrm{TB_{dn}} \\ + (1-\varepsilon)\mathrm{TB_{cos}}\exp(-2\tau\sec\theta) \end{aligned} \quad (2)$$

where T is the effective surface temperature, and ε is the effective canopy emissivity. The *effective* indicates a difference from actual temperature and emissivity since the surface canopy is modeled as an idealized single layer, different from actual canopies. τ is the vertical atmospheric optical depth; θ is the EIA, $\mathrm{TB_{up}}$ and $\mathrm{TB_{dn}}$ are atmospheric upwelling and downwelling emission, respectively; and $\mathrm{TB_{cos}}$ is the cosmic background.

A model for effective canopy emissivity is [2]

$$\varepsilon = a \times (f - 10.7)^2 + b \tag{3}$$

where f is the frequency in gigahertz, and a and b are constants to be determined; the parameter a is constrained to be negative. In this model, canopy emissivity increases at low frequency until 10.7 GHz because low frequency radiance is able to penetrate the forest canopy from the lower emissivity surface below, whereas high frequency radiance scatters more [2], [16], [17]. The two unknowns, a and b, can be determined using multiple channels. For instance, the five channels of WindSat from 19 to 37 GHz can be used to determine the two unknowns. This emissivity model does not account for angular dependence since both model and observation show that dense forests have small emissivity dependence on incidence angle [15], [17]. Macelloni *et al.* [17] compared airborne measurements with simulation, showing that forest emissivity is relatively flat as a function of incidence angle. Mo [15] showed that observed TBs from cross-track radiometer AMSU-A over Amazon rainforest have small angular dependence. The impact of angular dependence is further reduced when intercalibrating conical scanning radiometers, which often have close EIAs within a few degrees such as WindSat (50°–55°) and GMI (50°–53°).

The atmospheric emission terms at a given frequency are calculated as

$$\begin{aligned} \mathrm{TB_{up}} &= \int_0^{\mathrm{TOA}} T(z) \times \alpha(z) \times \sec\theta \times \exp\left(- \int_{z'}^{\mathrm{TOA}} \sec\theta \alpha(z') dz' \right) dz \\ \mathrm{TB_{dn}} &= \int_0^{\mathrm{TOA}} T(z) \times \alpha(z) \times \sec\theta \times \exp\left(- \int_0^{z} \sec\theta \alpha(z') dz' \right) dz \end{aligned} \tag{4}$$

where z is the vertical height, and α is the atmospheric absorption profile.

When intercalibrating different radiometers, it is convenient to define a reference and target radiometer [12], [23], [24]. Intercalibration evaluates the difference of the target radiometer with respect to the reference radiometer. Since the reference radiometer is not a perfect benchmark, intercalibration provides the relative rather absolute calibration. However, intercalibration is a critical method to diagnose new radiometer performance and reconcile constellation satellites. Equations (2)–(4) allow us to retrieve the surface emissivity using the reference radiometer and then simulate TBs for both reference and target radiometers, respectively. The double difference (DD) can characterize the difference between reference and target radiometers, i.e.,

$$\mathrm{DD} = (\mathrm{TB_{tar}} - \mathrm{TB_{tar,sim}}) - (\mathrm{TB_{ref}} - \mathrm{TB_{tar,sim}}) \tag{5}$$

where $\mathrm{TB_{tar}}$ and $\mathrm{TB_{ref}}$ are the actual observed TBs from the target and reference radiometers, respectively, and $\mathrm{TB_{tar,sim}}$ and $\mathrm{TB_{ref,sim}}$ are from the TOA TB model, respectively. A 1-D plane-parallel radiative transfer model (RTM) is used [11], [27]. The RTM is based on modules from previous research, in which the atmospheric absorption is given by Rosencrantz nitrogen [28] and water vapor [29], and Liebe liquid water [30] and oxygen [31].

A few filters are used for data quality control. The filter for screening precipitation is

$$\mathrm{TB_{19V}} - \mathrm{TB_{37V}} \leq 10K. \tag{6}$$

Greater scattering from precipitation at the higher frequency results in a decrease in the higher frequency radiance and therefore an increase the difference between $\mathrm{TB_{19V}}$ and $\mathrm{TB_{37V}}$ [14]. Filters for the single difference and DD are used to screen out data with anomalous observed or simulated TBs, i.e.,

$$\begin{aligned} (\mathrm{TB_{ref}} - \mathrm{TB_{ref,sim}}) &\leq 3K \\ (\mathrm{TB_{tar}} - \mathrm{TB_{tar,sim}}) &\leq 8K \\ \mathrm{DD} &\leq 8K. \end{aligned} \tag{7}$$

The TB range filters are used to screen out extreme high or low TBs, which can result from the presence of ice (cold TBs) or radio-frequency interference (warm TBs), i.e.,

$$\begin{aligned} 260K \leq \mathrm{TB_{ref}} &\leq 320K \\ 260K \leq \mathrm{TB_{tar}} &\leq 320K. \end{aligned} \tag{8}$$

The filter for retrieved surface emissivity is

$$0.7 \leq \varepsilon \leq 1. \tag{9}$$

Sufficiently sense forests have emissivity values above 0.9 [17]. Nonphysical retrieved emissivities above unity or below the lower bound thresholds can be caused by inaccurate representation of atmospheric emissions derived from ancillary data such as NCEP FNL data.

Intercalibration often requires collocating FOVs of the reference and target radiometers to a common region at the same time. Previous studies require collocation occurring within a $1^\circ \times 1^\circ$ grid box with 1-h time difference [9], [13], [32], [33]. These criteria are referred to as COL-1. The COL-1 method has been applied for both cold and warm calibration, where for warm calibration the two Amazon forest areas identified by Brown and Ruf [14] are used, with boundaries of latitude ranges $[-10^\circ, -5^\circ]$ and $[-5^\circ, -1^\circ]$, and longitude ranges of $[-74^\circ, -65^\circ]$ and $[-59^\circ, -53^\circ]$, respectively. We found that the collocation criteria such as the resolution of the grid box have significant impact on intercalibration. We studied this by changing the grid resolution and by comparing the results with COL-1 in Section III-C. In our collocation, if there are multiple TBs within a grid box from the reference or target radiometers, they are averaged before applying further intercalibration procedures. Accordingly, the scan position is also averaged. In practice, coarse grids (e.g., $1^\circ \times 1^\circ$) can have multiple TBs from an individual radiometer at any given grid box, whereas fine grids (e.g., $0.1^\circ \times 0.1^\circ$) only have a single TB.

D. Method to Examine Scan-Dependent TA and TB

In addition to intercalibration, the TA and TB from an individual radiometer can be used to examine its scan-dependent performance and improve APC and calibration corrections. TA and TB can be estimated for a specific forested region, which we will define later. In addition to filters in (1) and (6), a homogeneity filter is required for all of the channels

$$\mathrm{TB_{STD}} \leq 3K \tag{10}$$

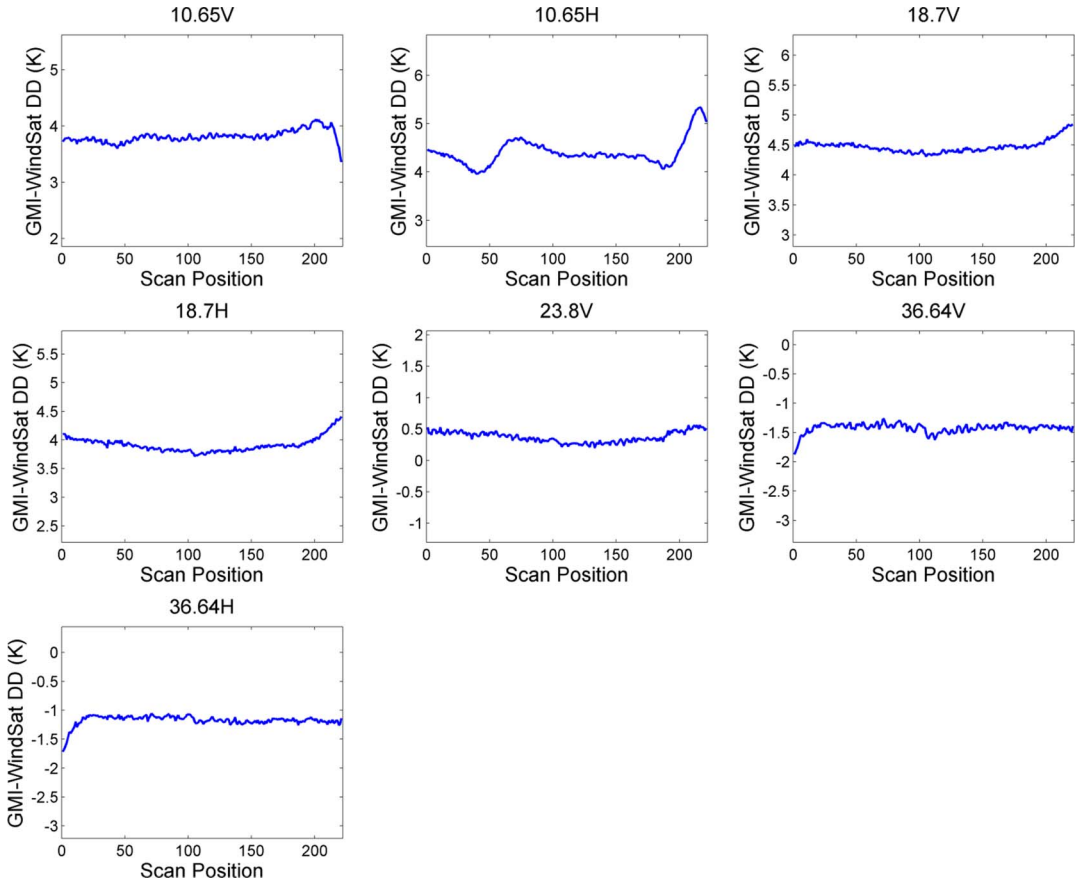


Fig. 3. GMI-WindSat along-scan DDs using the warm-scene calibration method. The along-scan information is obtained: the magnetic anomalies from scan position 50 to 100 at 10.65 V and 10.65 H polarizations, and the edge-of-scan anomalies at different channels.

where TB_{STD} is the standard deviation of TBs in each $1^\circ \times 1^\circ$ grid box for each channel. The filter threshold is empirically derived to screen out extreme surface inhomogeneity and precipitation that result in large TB standard deviation. Similar filters were applied in previous studies [9], [13]. After applying these filters, the TA and TB are averaged as a function of scan position.

III. Results From Boreal, Temperate, and Tropical Forests

A. Along-Scan Biases and Anomaly Detection

GMI along-scan performance for warm scenes is considered first. Fig. 3 shows the GMI and WindSat DD as a function of GMI scan position for each channel. Conical scanning radiometers conduct cross-track scanning by spinning the main reflector, where each revolution sees the cold sky reflector, hot load, and Earth scenes. The scan positions shown here represent the azimuthal positions for Earth scenes within each revolution. The most significant along-scan anomaly is noted at 10.65 H, where the DD first decreases from scan positions 0 to 50, then increases from 50 to 80, and tilts up again from 180 to 198 with a slightly drop from 198 to 221. A similar feature but with a smaller amplitude is also found at 10.65 V. Noticeable tilts on the right side of the scan position are seen at 18.7 V and 18.7 H. The edge-of-scan drop on the left side is noticed at 36.64 V and 36.64 H. The absolute value of DDs indicates that GMI has positive biases from 10.65 to 23.8 GHz and negative biases at 36.64 GHz.

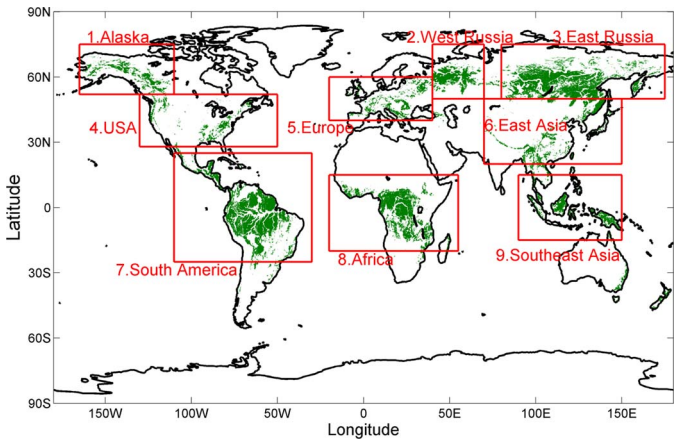


Fig. 4. Distribution of collocated calibration sites (green color) between GMI and WindSat. Nine subregions are defined for comparison: 1) Alaska; 2) West Russia; 3) East Russia; 4) United States; 5) Europe; 6) East Asia; 7) South America; 8) Africa; and 9) Southeast Asia. Regions 1–3 are boreal forests, 4–6 are temperate forests, and 7–9 are tropical forests.

These along-scan features and anomalies have been verified by different calibration teams, including the XCAL team, using methods such as prelaunch data, vicarious cold-end calibration, and deep-space maneuver [6], [10], [24]. Magnetic interference

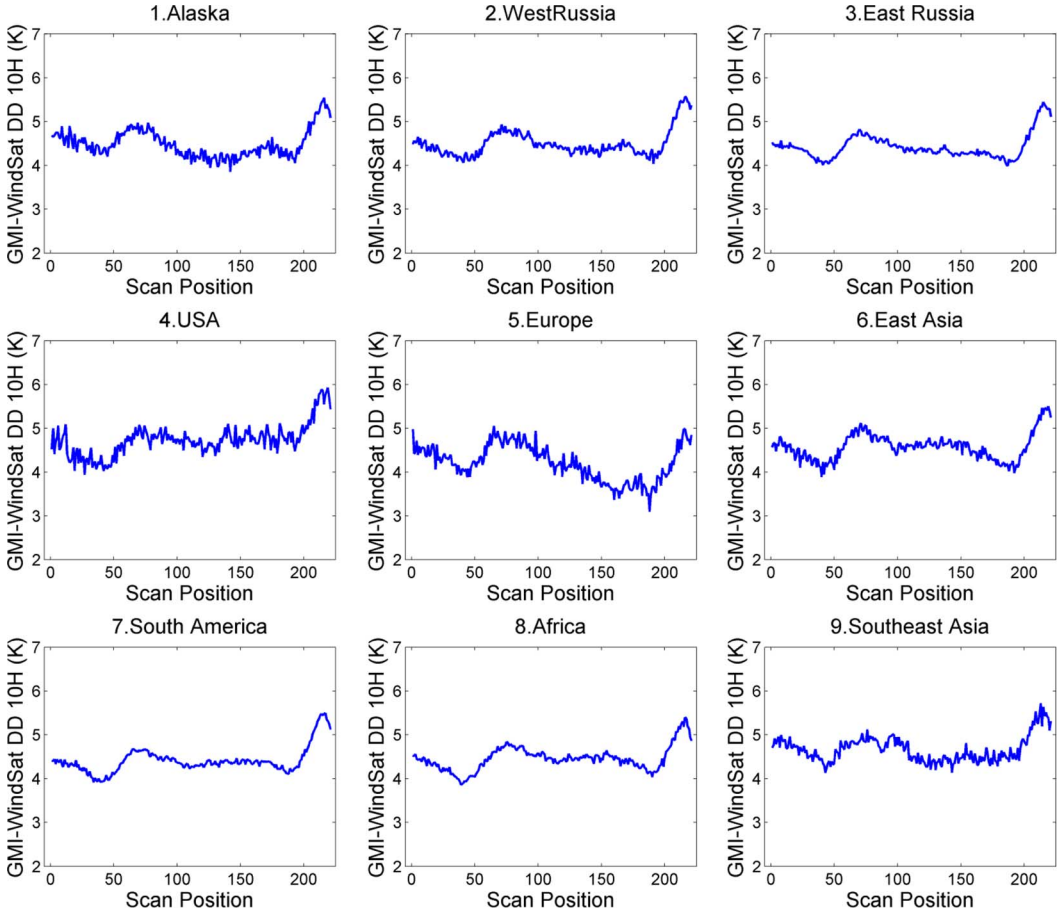


Fig. 5. Along-scan DDs at the 10.65H channel for the nine regions. The anomalies are reproduced in all of regions, with differences in fluctuation due to the number of samples.

is identified as the main cause of the feature observed around scan position 50 for 10.65H [6], [10], [24]. Intrusion is likely another reason for the observed edge-of-scan biases [6], [10], [24]. Similar along-scan features have also been found by prelaunch calibration, as well as vicarious cold-scene methods, verifying the strength of our methods [6], [10], [24]. These anomalies and biases, particularly the 10.65H magnetic feature, are useful tracers. They should be detected in different calibration sites. They can also be used to examine and improve the APC and along-scan corrections.

The distribution of vicarious calibration sites (green color) for GMI and WindSat intercalibration is shown in Fig. 4. We defined nine subregions to examine their performances. They represent boreal, temperate, and tropical regions, including: 1) Alaska (boreal); 2) West Russia (boreal); 3) East Russia (boreal); 4) Europe (temperate); 5) East Asia (temperate); 6) United States (temperate); 7) South America (tropical); 8) Africa (tropical); and 9) Southeast Asia (tropical).

Fig. 5 shows the DDs at 10.65 H channel for each of the nine regions. These regions all show the magnetic anomalies and edge-of-scan biases. The fluctuations, which vary region by region, mainly due to the number of samples, are considered in the succeeding section. The inland boreal and temperate regions, as well as coastal and island regions, show results consistent with the other regions. Similar to 10.65 H, the other channels also have consistent results among the nine regions.

Fig. 6 shows the along-scan DD using the COL-1 method over the Amazon rainforest. The along-scan fluctuation is so large that signals are indistinguishable. This is due to the coarse grid in COL-1, as well as the limited sample size from Amazon rainforests alone. Fig. 7 shows the impact of the sample size by comparing the detection of scan-dependent biases using only the Amazon rainforest sites versus using the global distribution of sites. The noise-like fluctuations in the case of the Amazon results, which are large enough to obscure small calibration biases, are significantly reduced when the global distributions is used. These results are considered in greater detail in Section III-C.

B. Analysis of Intercalibration Results

The mean DDs are presented in Table II. These numbers are overall consistent from region to region (differences within 0.2 K for most channels), confirming that boreal, temperate, and tropical forests can be used as high-quality vicarious calibration sites when using our method. In fact, even regions such as the Australian coastal forests provide consistent results, although they are not included in the nine regions. The number of collocations is given for each region, which is defined as the number of grid boxes in which FOVs are collocated.

Fig. 8 shows the change in samples size with respect to using the Amazon rainforest alone. The total number of data from this

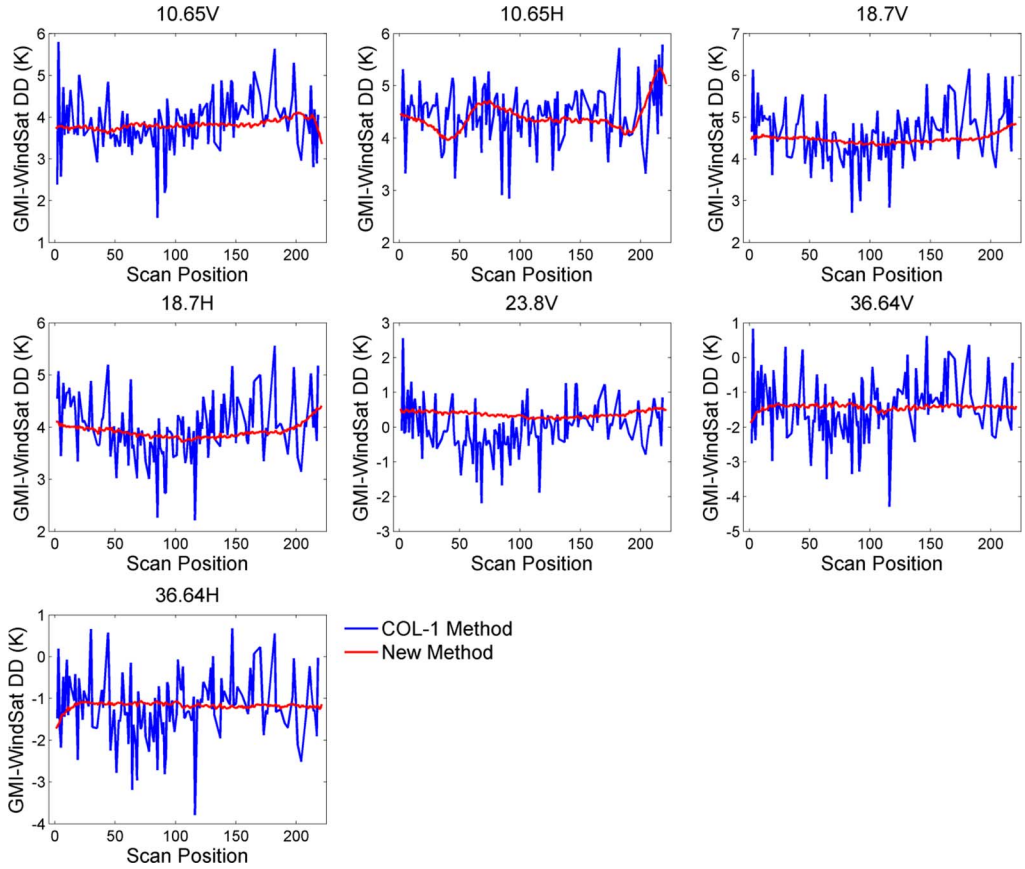


Fig. 6. Comparison of along-scan DDs between using the previous "COL-1" method and our new method. In COL-1 method, large fluctuations make along-scan signals indistinguishable.

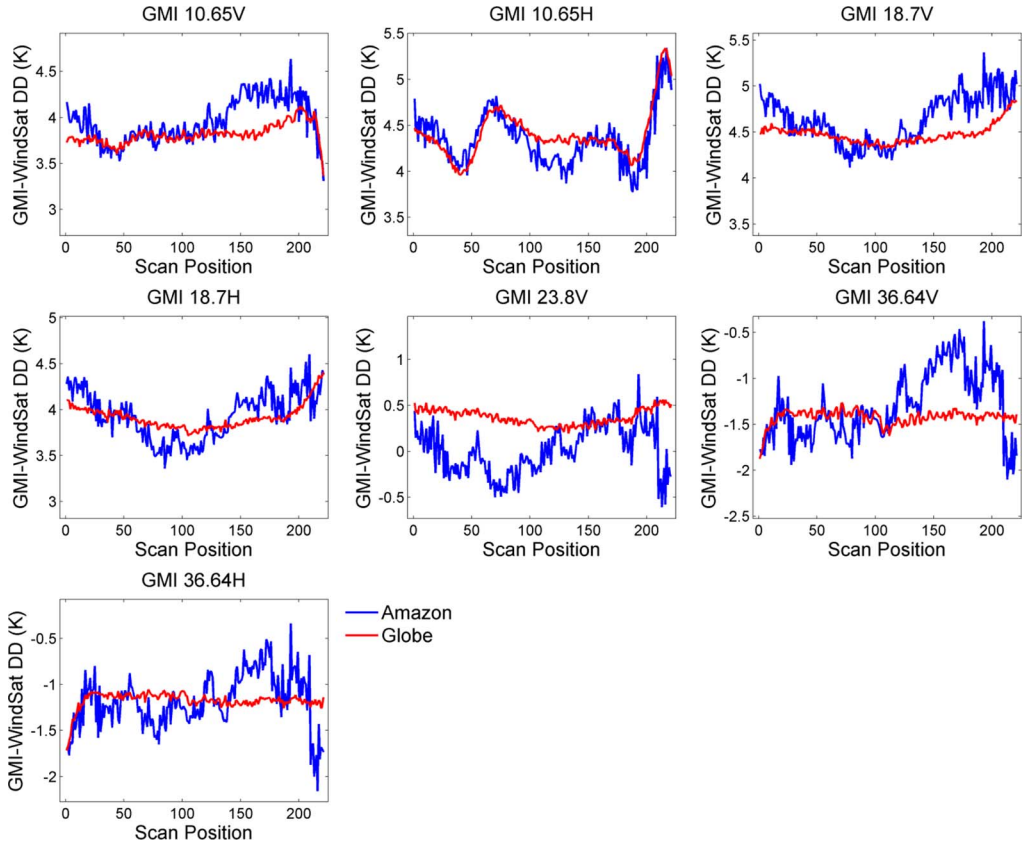


Fig. 7. Comparison of scan-dependent bias detection for warm TBs derived from DDs using only Amazon rainforest sites (blue) and global sites (red). Much large fluctuations result from using only Amazon rainforest sites because of their limited sample size.

TABLE II
GLOBAL AND REGIONAL MEAN DDS AS WELL AS NUMBER OF COLLOCATIONS BETWEEN GMI AND WINDSAT

	Global	Alaska	West Russia	East Russia	USA	Europe	East Asia	South America	Africa	SE Asia
No. Col.	433662	20230	44548	115661	11432	19389	28494	109688	58785	14899
10v	3.8	3.8	3.9	3.8	4.0	3.6	3.9	3.8	3.8	3.8
10h	4.4	4.3	4.4	4.3	4.6	4.1	4.5	4.4	4.4	4.6
19v	4.5	4.3	4.5	4.4	4.5	4.3	4.4	4.5	4.6	4.6
19h	3.9	3.9	3.9	3.8	4.1	4.0	3.8	3.9	4.0	3.9
23v	0.4	0.7	0.8	0.7	0.5	0.5	0.5	0.0	0.0	0.0
37v	-1.4	-1.4	-1.3	-1.3	-1.3	-1.4	-1.4	-1.6	-1.5	-1.6
37h	-1.2	-1.1	-1.1	-1.1	-1.0	-1.0	-1.1	-1.3	-1.2	-1.2

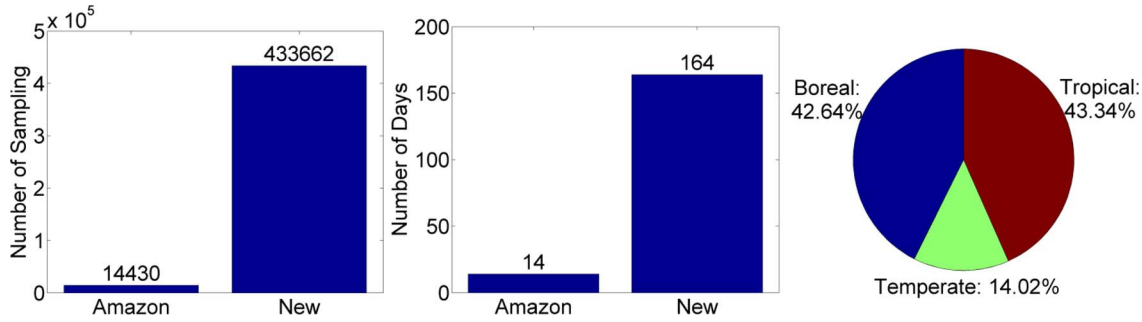


Fig. 8. Global forest vicarious warm calibration sites significantly increases the number of data in terms of total number (left) and number of days (middle), compared with the Amazon rainforest. The percentages of boreal, temperate, and tropical regions are also shown (right).

extended method is 433 662, which is 30 times more than that from the Amazon rainforest (14 430). The number of available days also increases from 17 to 164, out of a total of 181 possible days. Because of the order of magnitude increase, we are now able to monitor the near-daily GMI calibration status. Fig. 9 shows the daily mean time series of DDs. A continuous time series is obtained that is not possible using the Amazon region alone. The impact of water vapor on the time series can be seen. The time series indicates that the GMI performance is stable without noticeable drifting.

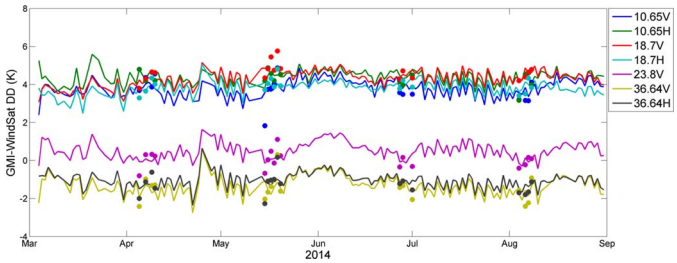


Fig. 9. GMI daily mean DDs for Mar–Aug 2014. The solid lines are from using the extended method (164 days available out of total 181 days), whereas solid circles are from the Amazon rainforest alone (17 days).

While the mean TBs in different regions are close to each other, high-latitude regions introduce colder scenes and expand the dynamic range of warm-scene TBs. Table III gives the mean GMI scene TBs corresponding to Table II. As an example, 10 H has mean TBs of (boreal) 276.8, 279.1, 279.0, (temperate) 282.7, 280.1, 279.9, (tropical) 282.6, 281.6, and 282.5 K for the nine regions, respectively, where boreal regions such as Alaska are around 5 K colder than tropical regions. Fig. 10 shows the histogram of TBs in each region. Boreal sites have more extreme cold TBs close to 260 K than tropical regions. Note that a filter has been used to limit the lower range of TBs to be 260 K. More dynamic TBs help examine the calibration dependence on TB.

Regional calibration differences are noted, which are most significant for the water vapor channels. As shown in Table II, the DDs at 23.8V channel are 0.7, 0.8, and 0.7 K in high-latitude boreal sites, Alaska, and West and East Russia, respectively. Middle-latitude temperate sites have closer numbers, e.g., 0.5 K in USA, Europe, and East Asia. However, tropical sites show very small DDs of < 0.1 K in South America, Africa, and Southeast Asia. A small but noticeable difference is seen at 37 V, which is affected by water vapor. As listed in Table I, WindSat and GMI have identical center frequency at the water vapor channel. However, they still have differences in EIA, local observing time, and bandwidth (see Table I), which affect observed TBs. While NCEP FNL data are used in computing the DD, it is known that uncertainty exists in these reanalysis data, and extensive studies have been performed to evaluate them [34], [35]. The observed latitudinal difference can result from either overestimation or underestimation of water vapor, biases in the vertical placement of the water vapor, inexact diurnal variations, etc. This, combined with the differences in instrument EIA and bandwidth, adds uncertainty to the DDs at this channel. Although the root cause is not identified in this paper, the clear latitudinal dependence implies that using

TABLE III
GLOBAL AND REGIONAL MEAN TBS OF GMI CORRESPONDING TO TABLE II

	Global	Alaska	West Russia	East Russia	USA	Europe	East Asia	South America	Africa	SE Asia
10v	281.9	278.5	280.6	280.6	284.2	281.7	281.2	283.8	282.9	283.4
10h	280.5	276.8	279.1	279.0	282.7	280.1	279.9	282.6	281.6	282.5
19v	285.3	282.5	284.0	284.5	287.5	284.6	284.4	287.1	286.0	286.4
19h	283.7	280.8	282.4	282.8	285.8	282.8	282.8	285.6	284.4	285.1
23v	282.9	279.2	280.5	281.3	284.4	281.2	281.9	285.6	284.4	284.7
37v	279.0	276.8	277.5	278.6	280.7	278.0	278.0	280.6	279.2	279.7
37h	278.0	275.6	276.6	277.5	279.5	276.7	277.0	279.9	278.4	279.2

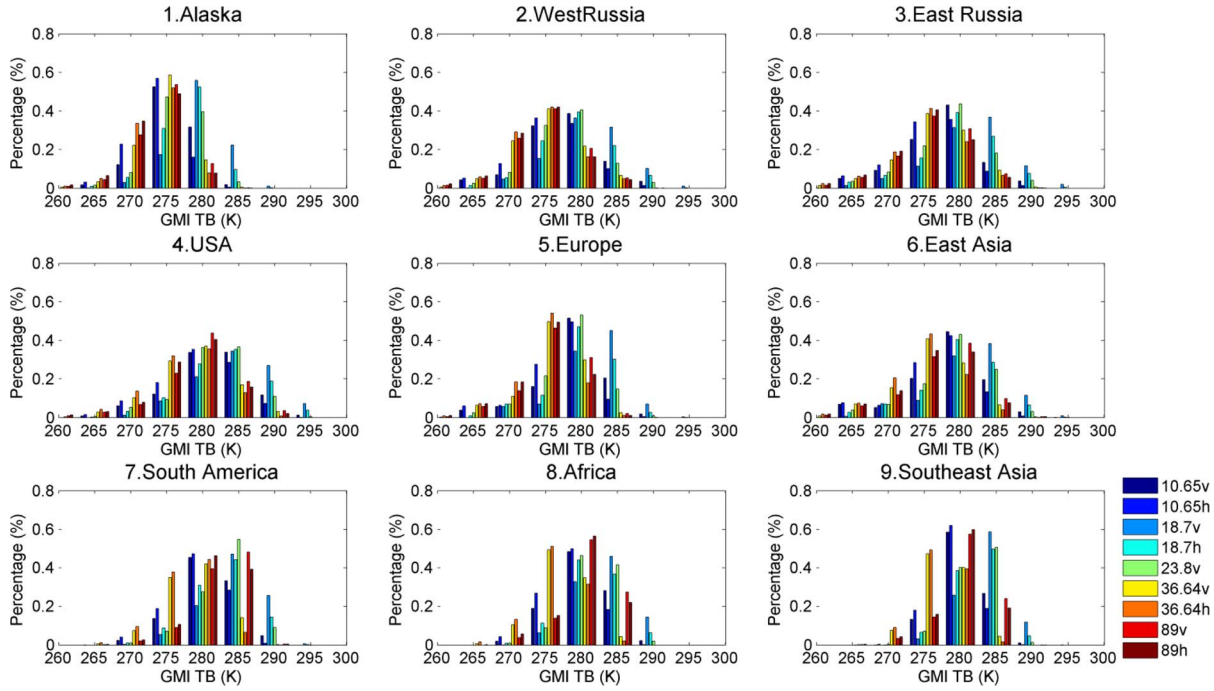


Fig. 10. TB histograms from different regions. Boreal and temperate regions provide colder TBs.

limited sites such as tropical Amazon rainforests alone could result in varying calibration biases outside of the tropics.

C. Impact of Grid Resolution on Intercalibration

We examine here the impact of grid resolutions on intercalibration. The FOVs of the reference and target radiometers are required to coincide in place and time. This is often implemented by dividing the Earth into subgrids. The size of a unit grid box determines how closely the FOVs match in space. The previous COL-1 method used a $1^\circ \times 1^\circ$ grid resolution, i.e., the Earth is divided into a $181\times$ 360 boxes, with the temporal collocation restricted to be within 1 h [9], [13], [32], [33].

A group of grid resolutions are examined, including $2^\circ \times 2^\circ$, $1^\circ \times 1^\circ$, $0.5^\circ \times 0.5^\circ$, $0.25^\circ \times 0.25^\circ$, $0.1^\circ \times 0.1^\circ$, and $0.05^\circ \times 0.05^\circ$. The time difference is kept the same at one hour. Fig. 11 shows an example of an along-scan DD comparison between $1^\circ \times 1^\circ$ and $0.1^\circ \times 0.1^\circ$ grids. The $1^\circ \times 1^\circ$ grid is very noisy, whereas the $0.1^\circ \times 0.1^\circ$ grid significantly reduces the noise so that along-scan features are discerned. Fig. 12 shows the comparison of $0.1^\circ \times 0.1^\circ$ to a finer resolution $0.05^\circ \times 0.05^\circ$. The $0.05^\circ \times 0.05^\circ$ grid is noisier because of the decrease in collocation data. Fig. 13 shows the 10.65H along-scan DDs at each grid resolution given above. Using the $0.1^\circ \times 0.1^\circ$ grid produces the best results. It should be noted that the $0.1^\circ \times 0.1^\circ$ grid is not a universal optimum. The choice of an optimal grid resolution can depend on radiometer specifications such as footprint size and scanning interval distance. It should also be noted that the actual size of a grid box is a function of latitude, i.e., smaller at higher latitude, since we use uniformly divided grids in the unit of degrees of latitude and longitude.

Further insights can be found in Table IV, which presents DDs and the number of collocations (collocated grid boxes) for different grid resolutions. The DDs change gradually with grid resolution at all channels. The 23.8V DD decreases from 0.58 K with $2^\circ \times 2^\circ$ to 0.29 K with $0.05^\circ \times 0.05^\circ$. The number of collocations increases when grid resolution decreases from $2^\circ \times 2^\circ$ to $0.1^\circ \times 0.1^\circ$, then decreases with smaller grid resolution. It should be noted that the number of collocations are defined as the number of collocated grid boxes, and the collocated TBs has been averaged at each grid box (if there are multiple TBs at each grid box) before applying intercalibration

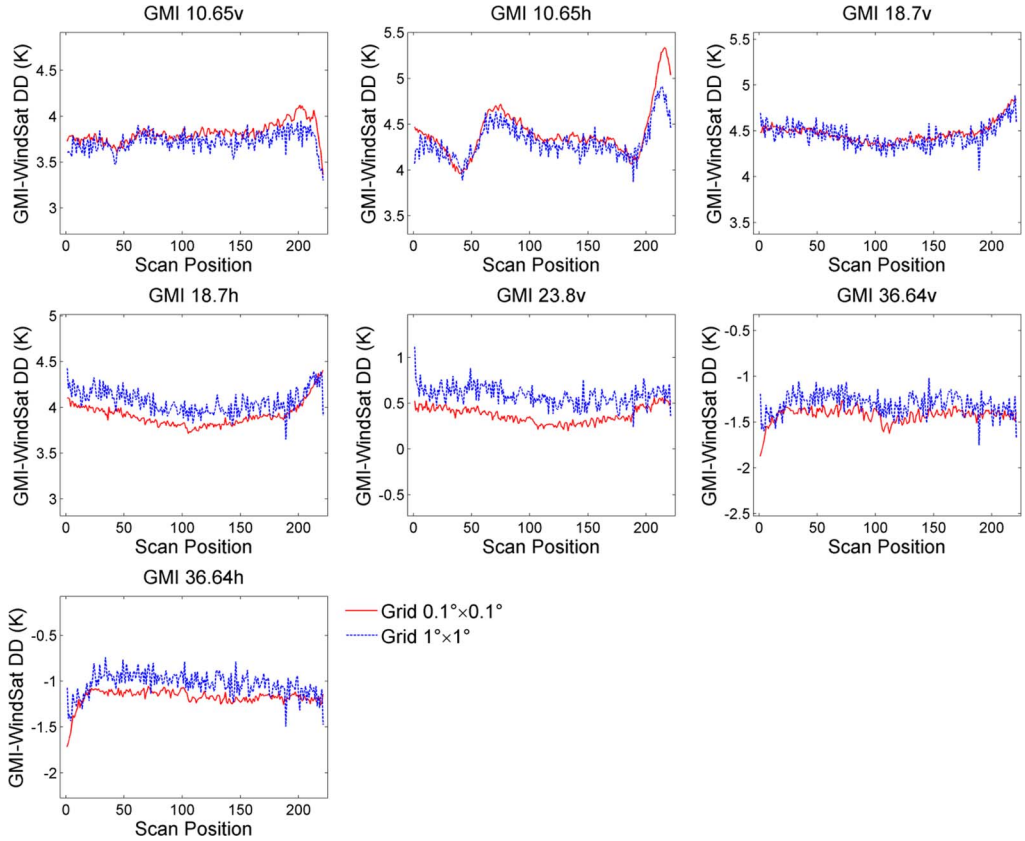


Fig. 11. Impact of grid resolution on along-scan calibration: $1^\circ \times 1^\circ$ versus $0.1^\circ \times 0.1^\circ$ (both use identified global forest sites with 1-hour intercalibration time difference). The absolute DD and degree of fluctuation change with grid resolution. Using $0.1^\circ \times 0.1^\circ$ grid gives more accurate DD and best resolves the along-scan information.

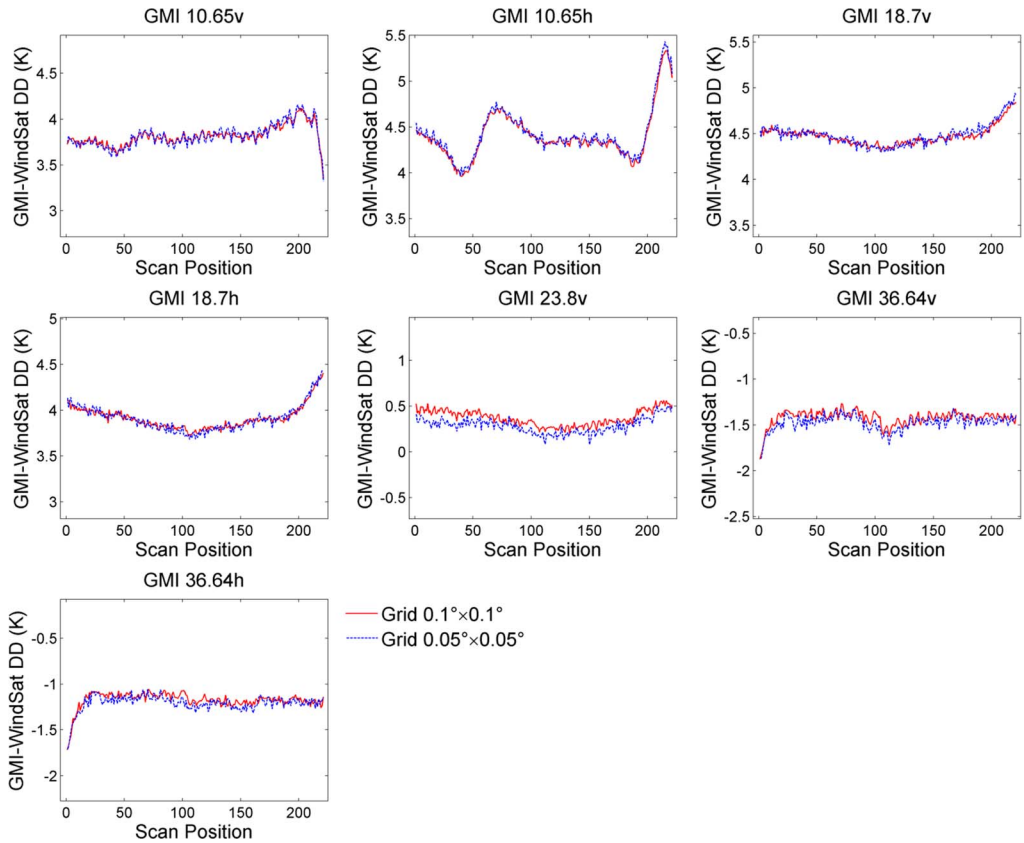


Fig. 12. Same as Fig. 11 but for $0.1^\circ \times 0.1^\circ$ versus $0.05^\circ \times 0.05^\circ$, where the $0.1^\circ \times 0.1^\circ$ grid is better.

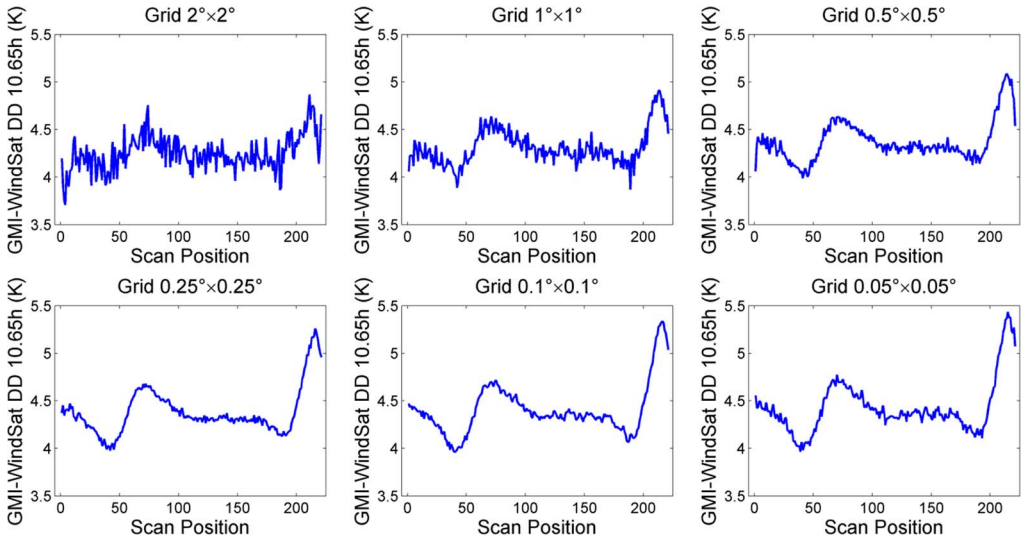


Fig. 13. 10.65H anomalies detected with different grid resolutions: $2^\circ \times 2^\circ$, $1^\circ \times 1^\circ$, $0.5^\circ \times 0.5^\circ$, $0.25^\circ \times 0.25^\circ$, $0.1^\circ \times 0.1^\circ$, and $0.05^\circ \times 0.05^\circ$, where grid $0.1^\circ \times 0.1^\circ$ is the best (they all use identified global forest sites with 1-hour intercalibration time difference). The identified global forest sites are used, and intercalibration time difference is 1 h.

TABLE IV
IMPACT OF GRID RESOLUTIONS ON DDS AND THE CORRESPONDING NUMBER OF COLLOCATIONS. USING THE $0.1^\circ \times 0.1^\circ$ GRID HAS THE MAXIMUM NUMBER OF COLLOCATIONS. THE ABSOLUTE VALUE OF DDS SHIFTS WITH GRID RESOLUTIONS

	Grid0.05	Grid0.1	Grid0.25	Grid0.5	Grid1	Grid2
No. Col.	195673	433662	210451	74424	27160	10362
10v	3.82	3.81	3.80	3.78	3.73	3.65
10h	4.44	4.40	4.38	4.38	4.33	4.27
19v	4.48	4.46	4.44	4.45	4.44	4.42
19h	3.91	3.90	3.96	4.04	4.06	4.05
23v	0.29	0.36	0.52	0.57	0.58	0.58
37v	-1.48	-1.42	-1.33	-1.30	-1.31	-1.32
37h	-1.21	-1.17	-1.08	-1.03	-1.03	-1.05

methods. The number of collocations first increases with finer grid because of the increase in the number of grid boxes, then decreases with extreme fine grid due to strict constrains for collocation since the distance between two FOVs from reference and target radiometers has a distribution that tails off toward small distance and has a minimum greater than zero.

These results indicate the importance of using appropriate grid resolution. The COL-1 method does not work well for warm-scene calibration because the use of a coarse grid resolution is vulnerable to land inhomogeneity. Finer grid resolutions better constrain the collocation of FOVs to the same scenes. On the other hand, grid resolutions cannot be arbitrarily small since there is always some distance between different FOVs. Too-fine grid resolutions can decrease the number of collocations significantly. Our method provides more accurate warm calibration because of the improvement of calibration techniques and more collocation for statistically robust constrains.

While results are not presented here, we also examined the impact of time differences on calibration. They have an insignificant impact on the along-scan and average DDs. For example, changing the time difference from 60 min to 30 min does not produce a noticeable effect.

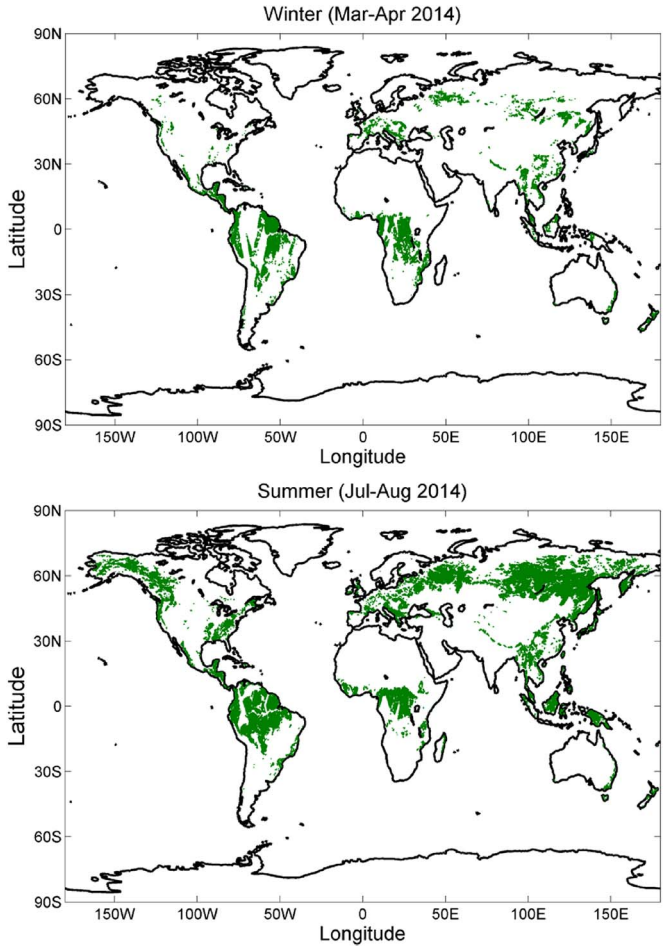


Fig. 14. Seasonal change in vicarious calibration sites, increasing in summer and decreasing in winter.

D. Seasonal Change of Ground Sites

A noteworthy seasonal change is observed at these vicarious calibration sites. Fig. 14 shows the distribution of available

TABLE V
CALIBRATION RESULTS IN WINTER (MARCH–APRIL 2014)

	Global	Alaska	West Russia	East Russia	USA	Europe	East Asia	South America	Africa	SE Asia
No. Col.	53006	93	1966	2278	459	2315	3893	23512	14712	985
10v	3.9	3.4	3.5	3.6	4.0	3.2	3.7	4.0	3.9	3.9
10h	4.5	4.1	4.1	4.3	4.5	3.7	4.6	4.5	4.5	4.5
19v	4.2	4.0	3.9	4.2	4.2	4.0	4.0	4.3	4.2	4.0
19h	3.7	3.7	3.5	3.9	4.0	3.9	3.6	3.7	3.7	3.6
23v	0.0	0.8	0.5	0.6	0.7	0.4	0.2	0.0	-0.2	-0.2
37v	-1.6	-1.2	-1.3	-1.1	-1.0	-1.5	-1.7	-1.6	-1.8	-1.7
37h	-1.3	-1.1	-1.0	-0.7	-0.6	-1.0	-1.2	-1.4	-1.5	-1.4

TABLE VI
CALIBRATION RESULTS IN SUMMER (JUL–AUG 2014)

	Global	Alaska	West Russia	East Russia	USA	Europe	East Asia	South America	Africa	SE Asia
No. Col.	218626	16307	29104	82676	7146	10424	14590	34498	15364	4993
10v	3.7	3.7	3.8	3.8	3.9	3.4	3.8	3.7	3.7	3.6
10h	4.3	4.3	4.3	4.3	4.6	4.0	4.6	4.3	4.3	4.5
19v	4.5	4.3	4.4	4.4	4.6	4.4	4.5	4.6	4.8	4.6
19h	3.9	3.9	3.9	3.9	4.1	4.0	3.9	3.9	4.0	3.8
23v	0.5	0.6	0.7	0.7	0.5	0.5	0.5	-0.1	0.2	-0.2
37v	-1.5	-1.5	-1.5	-1.4	-1.4	-1.6	-1.6	-1.7	-1.4	-1.9
37h	-1.2	-1.2	-1.2	-1.2	-1.0	-1.2	-1.2	-1.4	-1.2	-1.5

GMI-WindSat calibration sites in the Northern Hemisphere winter (March–April) and summer (July–August), respectively. A clear seasonal contrast is present. The contrast results from the summer green-up of boreal forest sites in the Northern Hemisphere through Alaska, Europe, and Russia, which almost disappears in winter. Temperate and tropical sites also have noticeable changes. Since the Southern Hemisphere has opposite seasons, green-up occurs in Southern Africa and Australia from March to April (winter in the Northern Hemisphere).

These season differences are further quantitatively illustrated in Tables V and VI. The available data increase from winter to summer, particularly for the Northern Hemisphere boreal sites. In winter, the numbers of collocation data are 93, 1966, and 2278 in Alaska and West and East Russia, respectively, whereas they are 16 307, 29 104, and 82 676 in summer. Regional differences still exist for the water vapor channels, both in winter and summer. Consequently, the 23.8V channel has a seasonal difference of 0.5 K between winter and summer.

The observed seasonal changes result from several causes. In temperate regions, the deciduous trees defoliate in winter, exposing the ground beneath the canopy. Since ground emission generally has a large polarization difference, our algorithm will automatically filter out those sites. In boreal regions, trees are generally evergreen coniferous species. They also shed needles but in a slower process. In addition, boreal sites have snow in winter, which increases the polarization difference. To verify this seasonal change, Fig. 15 shows the NDVI from MODIS in winter and summer of 2014, respectively. NDVI is a measurement of vegetation canopies based on chlorophyll-induced differences in near infrared and visible light [36]. The NDVI maps show a similar seasonal change of vegetation canopies.

The observed seasonal change has two implications. The available data would be very limited if calibration were based on fixed local regions, as used in the past. The seasonal shifting will cause the change of usable data in any specific region. The water vapor channels will be affected by the seasonal change since the seasonal change is related to the regional difference.

E. Using TA and TB Over Vicarious Forest Sites to Diagnose Calibration

Boreal, temperate, and tropical forest sites can be used to diagnose the performance of an individual radiometer. In particular, along-scan biases can be examined. Fig. 16 shows that the average GMI along-scan TBs over Africa. Along-scan magnetic anomalies and edge-of-scan biases are reproduced, similar to the DDs in intercalibration. In addition, a small along-scan signal is discerned, i.e., the sinusoid-like ripple with a peak-to-peak amplitude of 0.1 K. The ripple is related to mechanical scanning and has been observed in prelaunch testing [6]. In fact, the ripple feature is present in DD results (see Fig. 3), although not as clear as in the results shown here. For a specific region, more data are obtained from an individual radiometer compared with collocation-based methods that reduces data due to collocation constraints. The small signals are persistent throughout the scan position because they come from a larger region (Africa), rather than from averaging data over different small subgrids in intercalibration. Therefore, diagnosing data

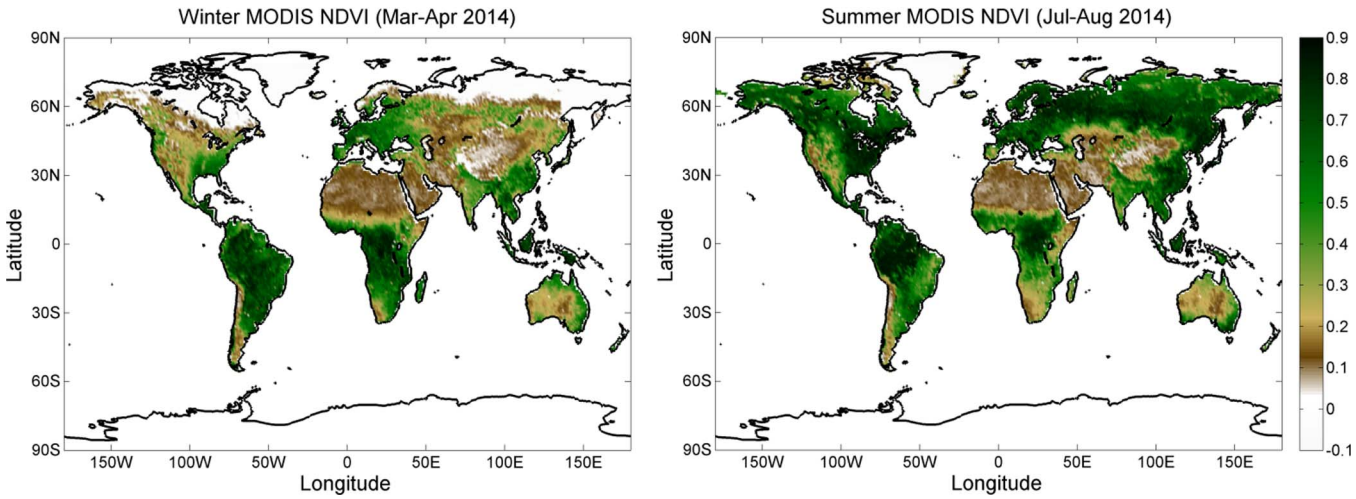


Fig. 15. MODIS NDVI in winter and summer, respectively, corresponding to Fig. 14. NDVI maps verify that there is a seasonal change in vegetation canopies [36].

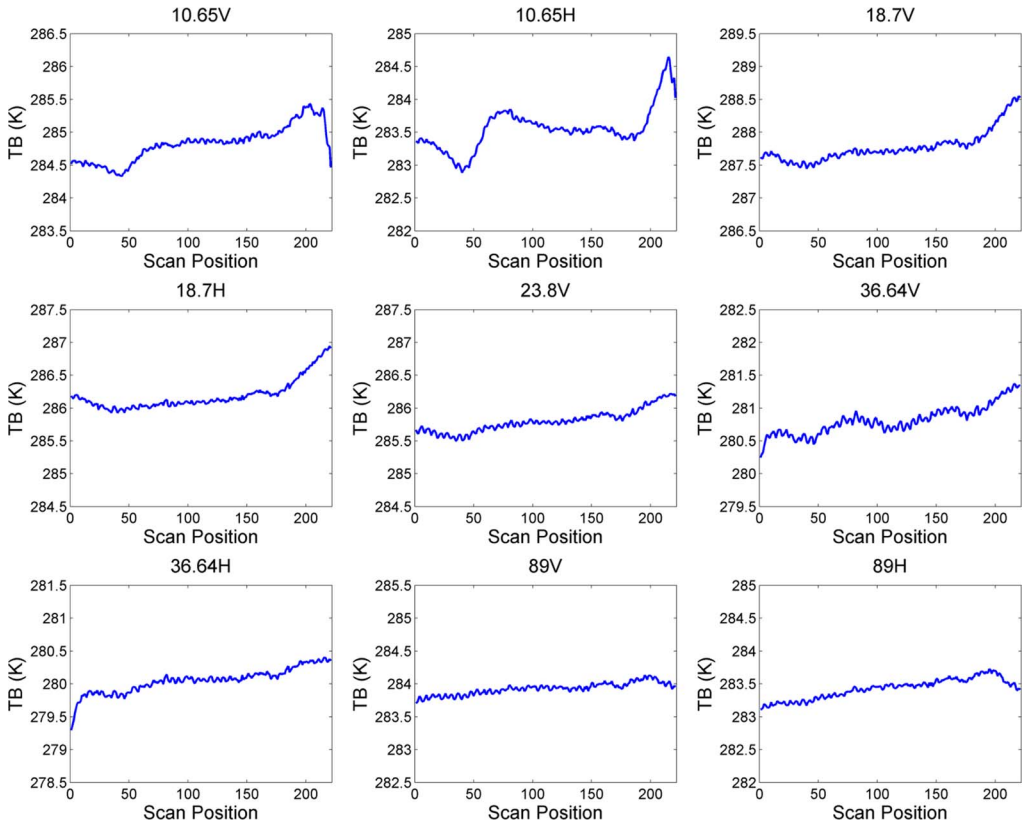


Fig. 16. Along-scan TBs for different GMI channels from the African calibration sites. The along-scan biases are similar to those detected by intercalibration. Additionally, the ripple signal with peak-to-peak amplitude of 0.1 K is discerned. It is also captured, but not as clearly, by the intercalibration method.

of an individual radiometer not only helps check the along-scan performance but can also provide additional information by discerning extremely small signals that would otherwise be indistinguishable due to noise in the intercomparison process.

Fig. 17 shows the corresponding along-scan TAs. The absolute value of TAs differs from that of the TBs because the APC is implemented in the latter. In addition to the difference of absolute values between TA and TB, there is a slight relative along-scan feature difference due to the APC. The APC, which is developed by Remote Sensing Systems [6], [10], uses prelaunch measured antenna pattern and RTM-based simulations that are combined to derive empirical coefficients for correcting spillover, reflector emissivity, cross-polarization, and along-scan anomalies. The along-scan TA further confirms the presence of anomalies, including the ripple. Without any empirical correction applied, the TAs provide direct information about instrumental performance and can be used to develop empirical correction for calibration issues. These warm-scene calibration results have been used and applied in GMI data for improving calibration performance.

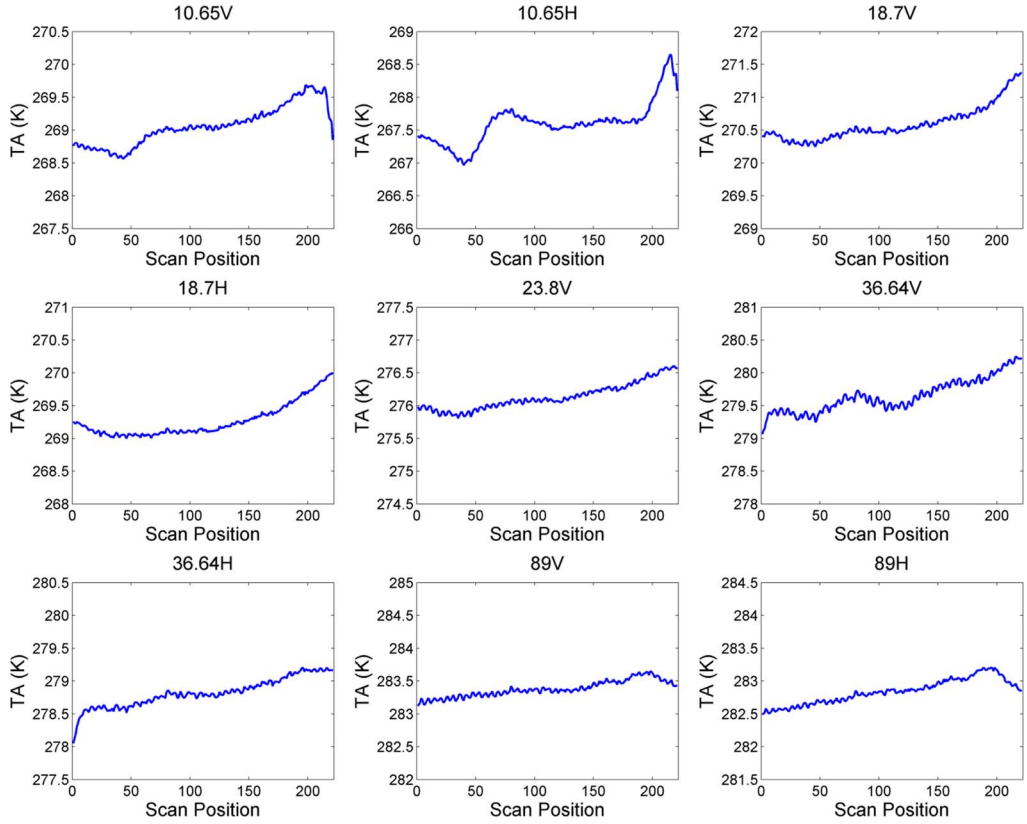


Fig. 17. Along-scan TA at different channels from African forest sites. It can be combined with TBs for correcting along-scan biases and improving the APC algorithm.

F. TB Gradient at Boreal Sites

While Section III-E shows the utility of using observed TAs and TBs to examine along-scan performance, a significant along-scan slope is observed in boreal sites. Fig. 18 shows the along-scan TBs over East Russia. A pronounced slope is seen in all channels. The along-scan features such as the magnetic anomaly and edge-of-scan biases are still noticeable because the slope acts as an additive signal. The along-scan slope is also noticeable in temperate and tropical sites (see Figs. 16 and 17) but not as significant as that in boreal sites.

The main cause is identified as the TBs' spatial gradient together with the GMI orbit geometry. Fig. 19 shows the mean TBs in East Russia corresponding to Fig. 18. A typical GMI swath is shown. GMI has an orbit inclination angle of 65°, and its conical scanning can cover higher latitudes up to 69.5°. In high-latitude regions, the GMI ground track is longitudinal, and its scan direction is latitudinal. Meanwhile, this region has a general latitudinal temperature gradient, with colder temperatures poleward. Because of the orbit geometry and TB gradient, the along-scan TBs tilt to one side of the scans. In low-latitude regions, temperature spatial gradient is relatively less pronounced, and the GMI track is no longer oriented longitudinally. It should be noted that the local time differences also affect the along-scan slope. GMI along-scan swath spans about 900 km, which has local time difference along the longitude, although to a much smaller degree. An example is he slightly along-scan slope over tropical Africa region as shown in Fig. 16, which is not as significant as that in boreal sites due to the latitudinal temperature gradients.

The slope can be removed by limiting region areas. For example, Fig. 20 shows the new along-scan TB within a small range of latitudes. The new boundaries have latitude ranges of $[50°, 51°]$ and longitude ranges of $[80°, 175°]$, whereas the original boundaries were $[50°, 75°]$ and $[80°, 175°]$. The slope is removed, although fluctuations increase due to a decrease in data volume. It should be noted that this latitudinal gradient is related to the low inclination of the GMI orbit.

IV. Conclusion

We find that boreal, temperate, and tropical forests are all potentially useful vicarious sites for warm-scene calibration. We present calibration methods for improving warm calibration, examining the scan-dependent performance, and correcting the APC algorithm (the along-scan correction is considered as an extended APC). For instance, the warm-end method can be used to examine and improve the calibration parameters that are empirically derived and tuned, which is a necessary complementary part to cold-end method over-ocean calibration to cover the full dynamic range of TBs. Our key findings are the following.

1) These sites can all be used for high-quality calibration. The introduction of boreal, temperate, coastal, and island

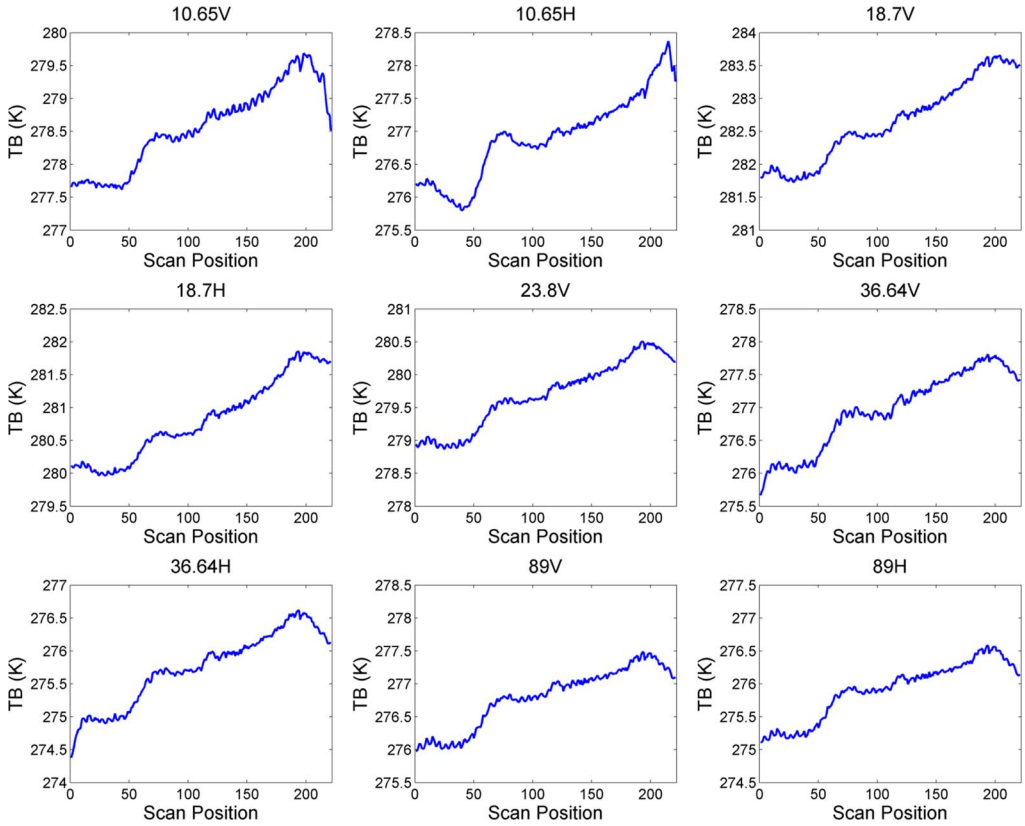


Fig. 18. Pronounced along-scan slope is present at boreal sites in East Russia. Similar slopes are found at other boreal sites but are not so significant at temperate and tropical sites.

sites significantly expands the calibration sites, allowing for near-global coverage. The TB dynamic range is extended to include colder TBs.

2) The addition of these new regions significantly increases the available data volume by a factor of ∼30 compared with using the Amazon rainforest alone. This allows for more statistically robust analysis and more continuous monitoring of radiometer performances, e.g., providing a near-daily calibration status for GMI in this paper.
3) These calibration sites have a noteworthy seasonal change, i.e., a green-up in summer and reduction in winter. The winter reduction is due to the tree defoliation and snow contamination. Our method is able to automatically filter out contaminated sites.
4) By using these worldwide calibration sites, regional differences are found, which are significant for water vapor channels and have a strong latitudinal dependence. Specifically, high and middle latitude regions, including boreal and temperate sites, yield similar calibration, which is different from tropical sites. The root cause is not conclusively identified. However, the clear presence of these differences implies that using limited sites, such as the Amazon rainforest alone, could result in latitudinal-dependent calibration biases.
5) Improved calibration techniques are developed, which overcome the problem of surface inhomogeneity. The grid resolution is found to significantly affect calibration. The $1^\circ \times 1^\circ$ grid size used in previous methods does not work well for the warm-scene calibration, losing scan-dependent features due to noise and shifting the absolute value of DDs. The $0.1^\circ \times 0.1^\circ$ resolution is found as an optimal choice for the specific radiometers in this paper.
6) We illustrate the technique by examining the performance of an individual radiometer using TB and TA data. This technique not only reproduces scan-dependent biases but also discerns extremely small signals, e.g., a scan-dependent calibration ripple with a peak-to-peak

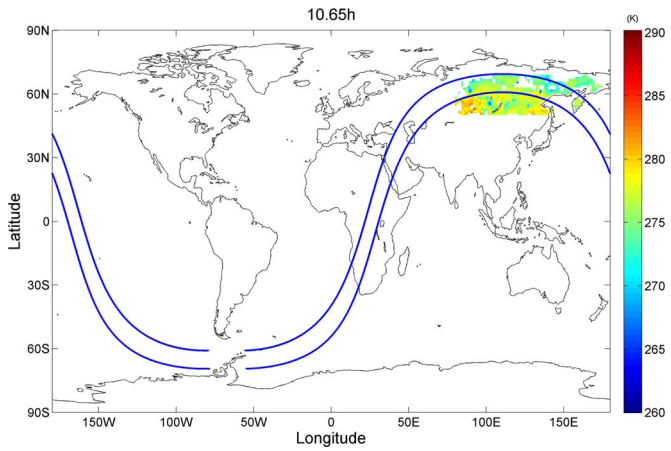


Fig. 19. Latitudinal temperature gradient and GMI orbit geometry result in the observed along-scan slope in Fig. 18. A typical GMI scanning swath (blue lines) show that GMI scans are latitudinal in boreal forest sites due to its low inclination orbit. In addition, boreal TBs (color coded) are latitude dependent, colder toward the poles. The two factors favor the along-scan slope, in addition to the effect of local time difference along the longitude.

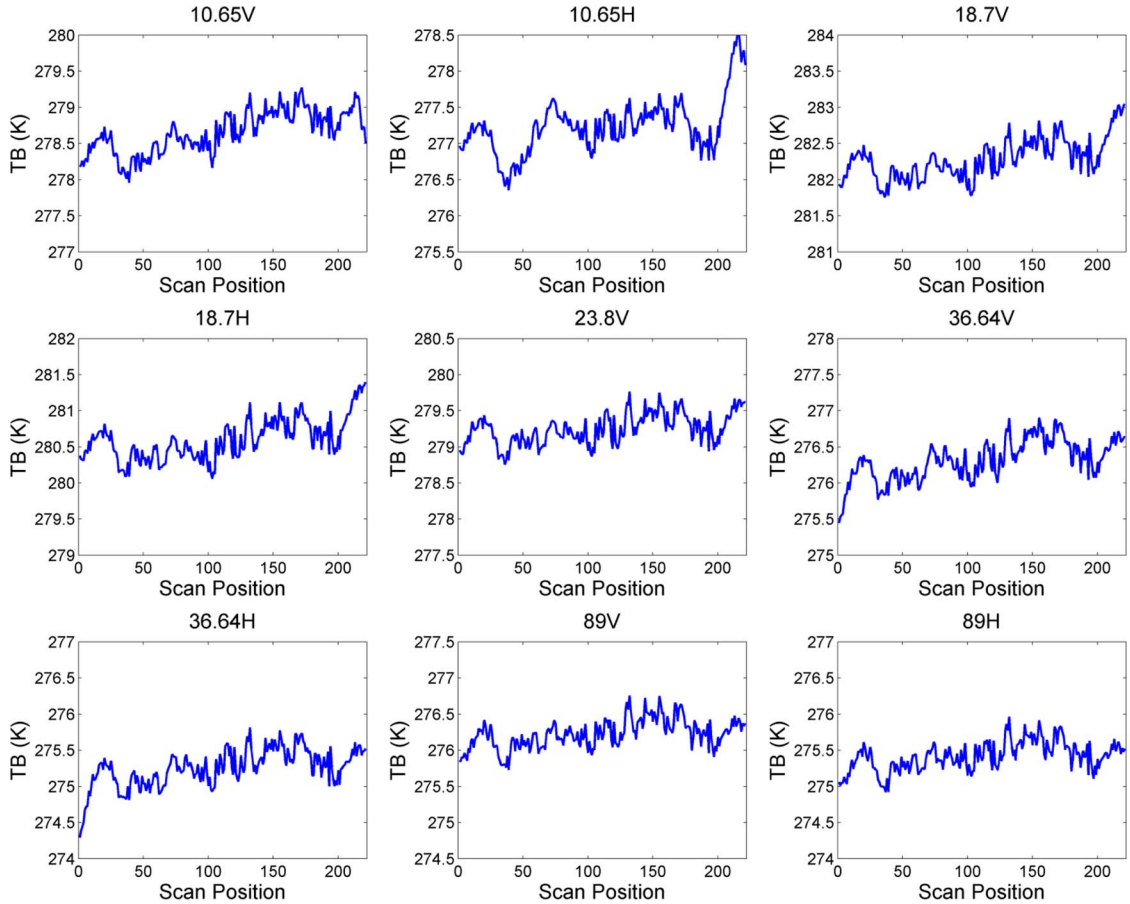


Fig. 20. Removing the along-scan slope in boreal forest sites by limiting the latitude range. The new boundaries have a latitude limit of $[50^\circ, 51^\circ]$ and a longitude limit of $[80^\circ, 175^\circ]$, compared to the original limits of $[50^\circ, 75^\circ]$ and $[80^\circ, 175^\circ]$.

amplitude of 0.1 K in GMI, which is also detected using the extended intercalibration method. This technique is able to diagnose and improve calibration, scan-dependent performance, and the APC algorithm.

7) When using TB and TA data, a distinct along-scan slope is noticed in boreal sites, which is not so significant in temperate and tropical regions. This is due to the latitudinal TB gradient together with the GMI low-inclination orbit, in addition to effect of local time difference. The slope can be removed by limiting the region area, such as the latitude range considered.

REFERENCES

[1] C. S. Ruf, "Detection of calibration drifts in spaceborne microwave radiometers using a vicarious cold reference," *IEEE Trans. Geosci. Remote Sens.*, vol. 38, no. 1, pp. 44–52, Jan. 2000.

[2] D. S. McKague, C. S. Ruf, and J. J. Puckett, "Beam spoiling correction for spaceborne microwave radiometers using the two-point vicarious calibration method," *IEEE Trans. Geosci. Remote Sens.*, vol. 49, no. 1, pp. 21–27, Jan. 2011.

[3] S. K. Biswas, K. Gopalan, W. L. Jones, and S. Bilanow, "Correction of time-varying radiometric errors in TRMM microwave imager calibrated brightness temperature products," *IEEE Geosci. Remote Sens. Lett.*, vol. 7, no. 4, pp. 851–855, Oct. 2010.

[4] K. Gopalan *et al.*, "A time-varying radiometric bias correction for the TRMM microwave imager," *IEEE Trans. Geosci. Remote Sens.*, vol. 47, no. 11, pp. 3722–3730, Nov. 2009.

[5] F. J. Wentz, P. Ashcroft, and C. Gentemann, "Post-launch calibration of the TRMM microwave imager," *IEEE Trans. Geosci. Remote Sens.*, vol. 39, no. 2, pp. 415–422, Feb. 2001.

[6] D. Draper, Calibration Data Book for Global Precipitation Measurement (GPM) Microwave Imager (GMI), Ball Aerospace & Technologies Corp. [Online]. Available: ftp://trmmopen.gsfc.nasa.gov

[7] J. X. Yang, D. S. McKague, and C. S. Ruf, "Identifying and resolving a calibration issue with GMI," in *Proc. IEEE IGARSS*, Milan, Italy, 2015.

[8] W. Berg, R. P. S. Mathew, H. Jennifer, and K. Christian, "Improved geolocation and earth incidence angle information for a fundamental climate data record of the SSM/I sensors," *IEEE Trans. Geosci. Remote Sens.*, vol. 51, no. 3, pp. 388–396, Mar. 2013.

[9] M. R. P. Sapiano, W. K. Berg, D. S. McKague, and C. D. Kummerow, "Toward an intercalibrated fundamental climate data record of the SSM/I sensors," *IEEE Trans. Geosci. Remote Sens.*, vol. 51, no. 3, pp. 1492–1503, Mar. 2013.

[10] D. Draper, D. Newell, F. Wentz, S. Krimchansky, and G. Skofronick-Jackson, "The Global Precipitation Measurement (GPM) Microwave Imager (GMI): Instrument overview and early on-orbit performance," *IEEE J. Sel. Topics Appl. Earth Observ. Remote Sens.*, vol. 8, no. 7, pp. 3452–3462, Jul. 2015.

[11] R. A. Kroodsma, D. S. McKague, and C. S. Ruf, "Inter-calibration of microwave radiometers using the vicarious cold calibration double difference method," *IEEE J. Sel. Topics Appl. Earth Observ. Remote Sens.*, vol. 5, no. 3, pp. 1006–1013, Jun. 2012.

[12] T. T. Wilheit, "Comparing calibrations of similar conically scanning window-channel microwave radiometers," *IEEE Trans. Geosci. Remote Sens.*, vol. 51, no. 3, pp. 1453–1464, Mar. 2013.

[13] S. K. Biswas *et al.*, "Intercalibration of microwave radiometer brightness temperatures for the global precipitation measurement mission," *IEEE Trans. Geosci. Remote Sens.*, vol. 51, no. 3, pp. 1465–1477, Mar. 2013.

[14] S. T. Brown and C. S. Ruf, "Determination of an Amazon hot reference target for the on-orbit calibration of microwave radiometers," *J. Atmos. Ocean. Technol.*, vol. 22, no. 9, pp. 1340–1352, Sep. 2005.
[15] T. Mo, "A study of the NOAA 16 AMSU-A brightness temperatures observed over Amazon rain forest," *J. Geophys. Res., Atmos.*, vol. 110, no. D23, Dec. 2005, Art. ID. D23102.
[16] P. Ferrazzoli and L. Guerriero, "Passive microwave remote sensing of forests: A model investigation," *IEEE Trans. Geosci. Remote Sens.*, vol. 34, no. 2, pp. 433–443, Mar. 1996.
[17] G. Macelloni, S. PALOScia, P. Pampaloni, and R. Ruisi, "Airborne multifrequency L- to Ka-band radiometric measurements over forests," *IEEE Trans. Geosci. Remote Sens.*, vol. 39, no. 11, pp. 2507–2513, Nov. 2001.
[18] P. W. Gaiser *et al.*, "The WindSat spaceborne polarimetric microwave radiometer: Sensor description and early orbit performance," *IEEE Trans. Geosci. Remote Sens.*, vol. 42, no. 11, pp. 2347–2361, Nov. 2004.
[19] W. L. Jones *et al.*, "Deep-space calibration of the WindSat radiometer," *IEEE Trans. Geosci. Remote Sens.*, vol. 44, no. 3, pp. 476–495, Mar. 2006.
[20] C. S. Ruf, Y. Hu, and S. T. Brown, "Calibration of WindSat polarimetric channels with a vicarious cold reference," *IEEE Trans. Geosci. Remote Sens.*, vol. 44, no. 3, pp. 470–475, Mar. 2006.
[21] A. Y. Hou *et al.*, "The global precipitation measurement mission," *Bull. Amer. Meteorol. Soc.*, vol. 95, no. 5, pp. 701–722, May 2014.
[22] Algorithm Theoretical Basis Document (ATBD), NASA Global Precipitation Measurement (GPM) Level 1C Algorithms, Version 1.3, Precipitation Processing System (PPS), NASA GSFC, Greenbelt, MD, USA, 2014, p. 211.
[23] T. T. Wilheit, "Intersatellite calibration of microwave radiometers for GPM," presented at the AGU Fall Meeting, San Fracisco, CA, USA, 2010, Paper H11L-07.
[24] GPM Intersatellite Calibration Working Group (XCAL), XCAL Meeting Report (2014 Jul. & 2015 Jan). [Online]. Available: http://www.gpm-x-cal.info/
[25] National Centers for Environmental Prediction National Weather Service NOAA U.S. Department of Commerce, NCEP FNL Operational Model Global Tropospheric Analyses, continuing from July 1999. [Online]. Available: http://dx.doi.org/10.5065/D6M043C6
[26] M. Shimada *et al.*, "Generation of 10m resolution PALSAR and JERS-SAR mosaic and forest/non-forest maps for forest carbon tracking," in *Proc. IEEE IGARSS*, 2011, pp. 3510–3513.
[27] J. X. Yang, D. S. McKague, and C. S. Ruf, "Land contamination correction for passive microwave radiometer data: Demonstration of wind retrieval in the great lakes using SSM/I," *J. Atmos. Ocean. Technol.*, vol. 31, no. 10, pp. 2094–2113, Oct. 2014.
[28] P. W. Rosenkranz, "Absorption of microwaves by atmospheric gases," in *Atmospheric Remote Sensing by Microwave Radiometry*, M. A. Janssen, Ed. New York, NY, USA: Wiley, 1993, pp. 37–90.
[29] P. W. Rosenkranz, "Water vapor microwave continuum absorption: A comparison of measurements and models," *Radio Sci.*, vol. 33, no. 4, pp. 919–928, Jul./Aug. 1998.
[30] H. J. Liebe, G. A. Hufford, and T. Manabe, "A model for the complex permittivity of water at frequencies below 1 THz," *Int. J. Infrared Millim. Waves*, vol. 12, no. 7, pp. 659–675, Jul. 1991.
[31] H. J. Liebe, P. W. Rosenkranz, and G. A. Hufford, "Atmospheric 60-GHz oxygen spectrum: New laboratory measurements and line parameters," *J. Quant. Spectrosc. Radiat. Transf.*, vol. 48, no. 5/6, pp. 629–643, Nov./Dec. 1992.
[32] N. N. Das, A. Colliander, S. K. Chan, E. G. Njoku, and L. Li, "Intercomparisons of brightness temperature observations over land from AMSR-E and WindSat," *IEEE Trans. Geosci. Remote Sens.*, vol. 52, no. 1, pp. 452–464, Jan. 2014.
[33] A. Okuyama and K. Imaoka, "Intercalibration of the advanced microwave scanning radiometer-2 (AMSR2) level-1B dataset," in *Proc. 13th Spec. Meet. MicroRad Remote Sens. Environ.*, 2014, pp. 205–206.
[34] L. Bengtsson *et al.*, "The need for a dynamical climate reanalysis," *Bull. Amer. Meteorol. Soc.*, vol. 88, no. 4, pp. 495–501, Apr. 2007.
[35] D. T. Kleist *et al.*, "Introduction of the GSI into the NCEP Global data assimilation system," *Weather Forecasting*, vol. 24, no. 6, pp. 1691–1705, Dec. 2009.
[36] A. Huete *et al.*, "Overview of the radiometric and biophysical performance of the MODIS vegetation indices," *Remote Sens. Environ.*, vol. 83, no. 1/2, pp. 195–213, Nov. 2002.



John Xun Yang (S'11) received the Bachelor's (first class honors) and Master's degrees from Sichuan University, Chengdu, China, and the City University of Hong Kong, Hong Kong, respectively. He is currently working toward the Ph.D. degree at the University of Michigan, Ann Arbor, MI, USA. Before coming to the University of Michigan, he worked from 2010 to 2011 at the Hong Kong University of Science and Technology, Hong Kong.

His research interest is Earth remote sensing. He is part of the Global Precipitation Measurement (GPM) Mission Intercalibration Team. He has developed and published a number of methods on radiometer calibration and its science application. Additionally, he has done engineering work on building up an L-band radiometer and accessory hardware and software tools to calibrate GPS simulators for the Cyclone Global Navigation Satellite System (CYGNSS) mission. He has experience using Lidar to measure atmospheric aerosol including instrument development, calibration, and retrieval algorithm development.



Darren S. McKague (M'08) received the Ph.D. degree in astrophysical, planetary, and atmospheric sciences from the University of Colorado, Boulder, CO, USA, in 2001.

He is currently an Associate Research Scientist with the Department of Climate & Space Sciences and Engineering at the University of Michigan, Ann Arbor, MI, USA. Prior to working for Michigan, he worked as a Systems Engineer with Ball Aerospace and with Raytheon, and as a Research Scientist with Colorado State University, Fort Collins, CO, USA. His experience with remote sensing hardware includes systems engineering for several advanced passive and active instrument concepts and the design of the calibration subsystem on the Global Precipitation Mission (GPM) Microwave Imager (GMI) and the development of calibration and intercalibration techniques for the GPM constellation. His algorithm experience includes the development of a near-real-time algorithm for the joint retrieval of water vapor profiles, temperature profiles, cloud liquid water path, and surface emissivity for the Advanced Microwave Sounding Unit, Colorado State University, Fort Collins, CO, USA, and the development of the precipitation rate, precipitation type, sea ice, and sea surface wind direction algorithms for the risk reduction phase of the Conical scanning Microwave Imager/Sounder. His research interests include remote sensing with emphases on the development of spaceborne microwave remote sensing hardware, passive microwave calibration techniques, and mathematical inversion techniques for geophysical retrievals.



Christopher S. Ruf (S'85–M'87–SM'92–F'01) received the B.A.degree in physics from Reed College, Portland, OR, USA, and the Ph.D. degree in electrical and computer engineering from the University of Massachusetts, Amherst, MA, USA.

He is currently a Professor of atmospheric science and electrical engineering, University of Michigan, Ann Arbor, MI, USA. He has worked previously at Intel Corporation, Hughes Space and Communication, NASA Jet Propulsion Laboratory, and Pennsylvania State University, State College, PA, USA. His research interests include Global Navigation Satellite System-R bistatic scatterometry, microwave radiometry, atmosphere and ocean geophysical retrieval algorithm development, and sensor technology.

Dr. Ruf served as the Editor-in-Chief of the IEEE TRANSACTIONS ON GEOSCIENCE AND REMOTE SENSING (IEEE TGRS) and has served on the editorial boards of *Radio Science* and the *Journal of Atmospheric and Oceanic Technology*. He received four NASA Certificates of Recognition and seven NASA Group Achievement Awards, and the 1997 IEEE TGRS Best Paper Award, the 1999 IEEE Resnik Technical Field Award, the 2006 International Geoscience and Remote Sensing Symposium Best Paper Award, and the 2014 Geoscience and Remote Sensing Society Outstanding Service Award. He is a member of the American Geophysical Union, the American Meteorological Society, and the Commission F of the Union Radio Scientifique Internationale.